Inorganic Chemistry
Cite This: Inorg. Chem. XXXX, XXX, XXX–XXX
Article
pubs.acs.org/IC

Single-Crystal α-Fe_2O_3 with Engineered Exposed (001) Facet for High-Rate, Long-Cycle-Life Lithium-Ion Battery Anode

Pingge He,[†] Zhengping Ding,[‡] Xudong Zhao,[†] Jiahao Liu,[†] Shuanglei Yang,*[,§] Peng Gao,[‡] and Li-Zhen Fan*[,†]

[†]Beijing Advanced Innovation Center for Materials Genome Engineering, Institute of Advanced Materials and Technology, University of Science and Technology Beijing, Beijing 100083, China

[‡]International Center for Quantum Materials, and Electron Microscopy Laboratory, School of Physics, Peking University, Beijing 100871, China

[§]School of Material Science and Engineering, Qingdao University, Qingdao 266071, China

Supporting Information

ABSTRACT: Designing electrode materials with engineered exposed facets provides a novel strategy to improve their electrochemical properties. However, the controllability of the exposed facet remains a daunting challenge, and a deep understanding of the correlation between exposed facet and Li^+-transfer behavior has been rarely reported. In this work, single-crystal α-Fe_2O_3 hexagonal nanosheets with an exposed (001) facet are prepared with the assistance of aluminum ions through a one-step hydrothermal process, and structural characterizations reveal an Al^{3+}-concentration-dependent-growth mechanism for the α-Fe_2O_3 nanosheets. Furthermore, such α-Fe_2O_3 nanosheets, when used as lithium-ion battery anodes, exhibit high specific capacity (1261.3 mAh g^{-1} at 200 mA g^{-1}), high rate capability (with a reversible capacity of approximately 605 mAh g^{-1} at 10 A g^{-1}), and excellent cyclic stability (with a capacity of over 900 mAh g^{-1} during 500 cycles). The superior electrochemical performance of α-Fe_2O_3 nanosheets is attributed to the pseudocapacitive behavior, Al-doping in the α-Fe_2O_3 structure, and improved Li^+-transfer property across the (001) facet, as elucidated by first-principles calculations based on density functional theory. These results reveal the underlying mechanism of Li^+ transfer across different facets and thus provide insights into the understanding of the excellent electrochemical performance.

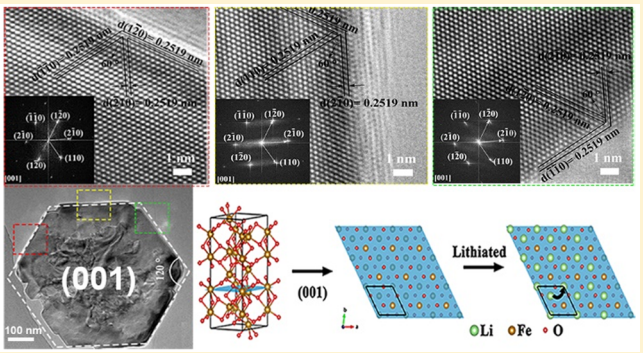

1. INTRODUCTION

During recent decades, synthesis of nanomaterials with desirable exposed facets has elicited much attention in various fields such as catalysis, photocatalysis and energy storage systems due to their unique physical-chemical properties.[1−3] Particularly, for lithium-ion batteries (LIBs), anodes with specific exposed facets have been highly developed and demonstrated to exhibit superior electrochemical performance.[4] Lou et al. reported that TiO_2 with nearly 100% exposed (001) facets exhibited a fast lithium ion storage with a reversible capacity of 150 mAh g^{-1} even at a high current rate of 10 C (1700 mA g^{-1}). The improved rate capability of electrodes is attributed to the lower energy barrier for surface transmission of Li^+ across the (001) facet of TiO_2.[5] Moreover, intensive efforts have also been made to investigate the influence of exposed facets of nanostructures (e.g., Co_3O_4,[6,7] SnO_2)[8,9] on the Li-ion storage properties, demonstrating that the exposed facet plays a crucial role in Li-ion transfer and consequently influencing the electrochemical performances of electrodes.[10,11] Essentially, the performance of LIB anodes is determined by the thermodynamic and kinetic behavior of Li ions, which is strongly related to the exposed facet of electrodes.[12,13] Therefore, rational designs of electrode structure with controllable exposed facets are needed to meet the increasing demand for high-performance LIB anodes.

Among all LIB anodes, α-Fe_2O_3 has been considered one of the most promising candidates for next-generation anode materials due to its high theoretical specific capacity (1006 mAh g^{-1}), abundance as a natural resource, nontoxicity, high corrosion resistance, and low cost.[14−16] Moreover, α-Fe_2O_3 could be controllably synthesized with various morphologies (nanoparticle, nanowire, nanorod, nanocube, nanosphere, etc.),[17−19] which provides an effective way to realize the structural and functional diversity of anodes to meet the practical requirements. However, Fe_2O_3-based anodes generally suffer low rate capability and poor cyclic stability, severely limiting their practical applications in LIBs.[20,21] Many

Received: June 2, 2019

DOI: 10.1021/acs.inorgchem.9b01626
Inorg. Chem. XXXX, XXX, XXX–XXX

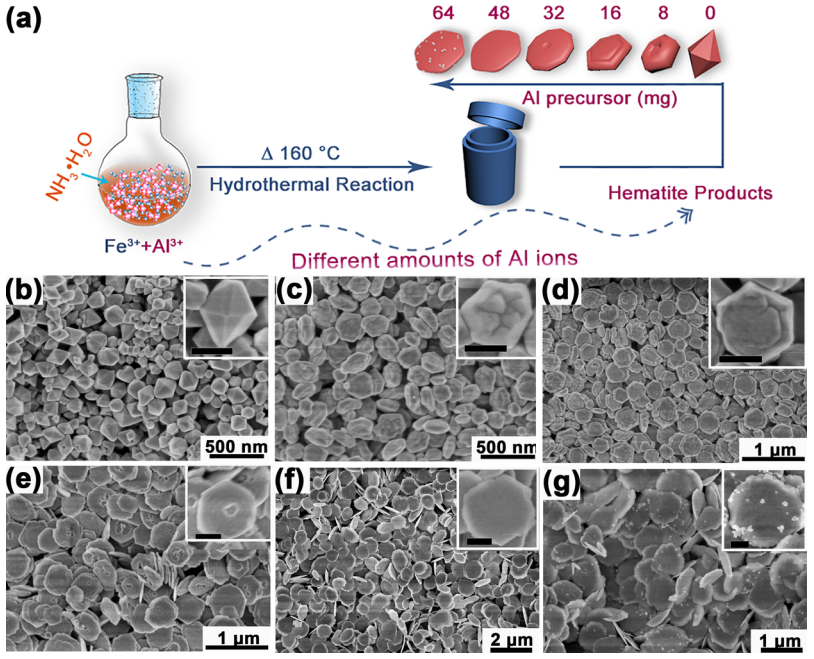

Figure 1. (a) Schematic illustration of the fabrication process of α-Fe_2O_3; SEM images of α-Fe_2O_3 prepared under different Al ion concentrations: (b) S1, (c) S2, (d) S3, (e) S4, (f) S5, and (g) S6 samples, respectively (the inset bar is 200 nm).

approaches to compositing with other materials are proposed to improve the electrochemical performance of Fe_2O_3-based anodes,[22−24] which might also feature complicated preparation processes. More recently, some research work has been focused on the synthesis of α-Fe_2O_3 with differently exposed facets for LIB applications, which has been demonstrated as a productive approach to improve the electrochemical property of Fe_2O_3.[25] In that work, the outstanding performance could be the synergistic effect between graphene and α-Fe_2O_3 (012). Controllable and tailorable ion/electron transfer characteristics in Fe_2O_3 electrodes with engineered exposed facets are of great significance for electrodes to realize the high levels of charge storage within short periods of time (high rate capability). However, a deep understanding of fundamental of the exposed facet-related Li^+-transfer behavior, which is imperative to achieve high-performance and durable LIB anodes, has been rarely reported. Moreover, the controllability of specific exposed facets during synthesis process remains an unmet challenge.

In this work, we have developed a facile one-step hydrothermal method with the assist of Al-ion additive to fabricate single-crystal α-Fe_2O_3 hexagonal-like nanosheets with nearly 100% exposed (001) facet. Under alkali condition, Al ions exhibit empty 3p and 3s orbitals, which allows them to easily connect with the lone-pair electrons on the hydroxyl, consequently forming a aluminum hydroxide precipitate. However, in a high-concentration ammonia−water solution, the aluminum hydroxide precipitate could ionize into aluminum ions. Meanwhile, the oxygen-coordination ability of lone pair electrons with nitrogen is stronger than that with hydroxyl, leading to the formation of an aluminum ammonia solution.[26] Extra aluminum ions would be adsorbed to the α-Fe_2O_3 surface and subsequently restrain the growth of α-Fe_2O_3 along the z-axis, consequently affecting the morphology (exposed facet) of α-Fe_2O_3 products.[27] The growth mechanism of α-Fe_2O_3 with controllable exposed facets was revealed based on a set of Al ion concentration-dependent experiments combined with theoretical simulations. As for LIB anode application, the as-prepared α-Fe_2O_3 hexagonal nanosheet with an engineered exposed (001) facet exhibits high reversible capacity, high rate capability, and excellent cyclic stability. Moreover, the correlation between the electrochemical performance and the exposed facet is investigated in depth based on both experimental data and simulations to elucidate the underlying mechanism of Li^+ transfer across different facets.

2. EXPERIMENTAL SECTION

2.1. Materials. Iron(III) nitrate nonahydrate ($Fe(NO_3)_3{\cdot}9H_2O$, AR) and ammonia solution (25%, AR) were purchased from Sinopharm Chemical Reagent Co., Ltd., Aluminum acetate basic ($Al(OH)C_4H_6O_4$, AR) was purchased from Shanghai Jingchun Chemical Reagent Co., Ltd. All the materials were used without further purification during the whole experimental process.

2.2. Controllable Synthesis of Single-Crystal α-Fe_2O_3. Single-crystal α-Fe_2O_3 was prepared by a facile hydrothermal process. Typically, 2 mmol of $Fe(NO_3)_3{\cdot}9H_2O$ was dissolved in 10 mL of water under magnetic stirring, and then aluminum acetate basic was added. To investigate the growth mechanism, the aluminum acetate basic with a mass of 0 (labeled as S1), 8 (S2), 16 (S3), 32 (S4), 48 (S5), and 64 mg (S6) was added in the above solution, respectively. The solution was stirred for 10 min, and after that 10 mL of ammonia solution was added. The mixture was continuously stirred and subsequently transferred into a Teflon-lined stainless-steel autoclave with a capacity of 50 mL. The autoclave was sealed and kept at 160 °C for 2, 4, 8, and 12 h, respectively. After the hydrothermal process, the autoclave was cooled down to room temperature. The products were collected by centrifugation, washing with deionized water, and ethanol, and then drying at 80 °C under vacuum.

2.3. Characterization. X-ray diffraction (XRD) analyses were carried out by a D/ruanx 2550PC (Japan) using Cu Ka radiation (λ = 0.1542 nm). X-ray photoelectron spectrometry (XPS) was performed on a Thermo Fisher (ESCALAB 250Xi) photoelectron spectrometer. Scanning electron microscopy (SEM) was carried out using a Hitachi S4800 scanning electron microscope. Transmission electron microscopy (TEM) analyses were performed on a FEI Tecnai G2 F20 at 200 kV with an Oneview IS (Gatan) camera and Oxford X-Max^N TSR

DOI: 10.1021/acs.inorgchem.9b01626
Inorg. Chem. XXXX, XXX, XXX−XXX

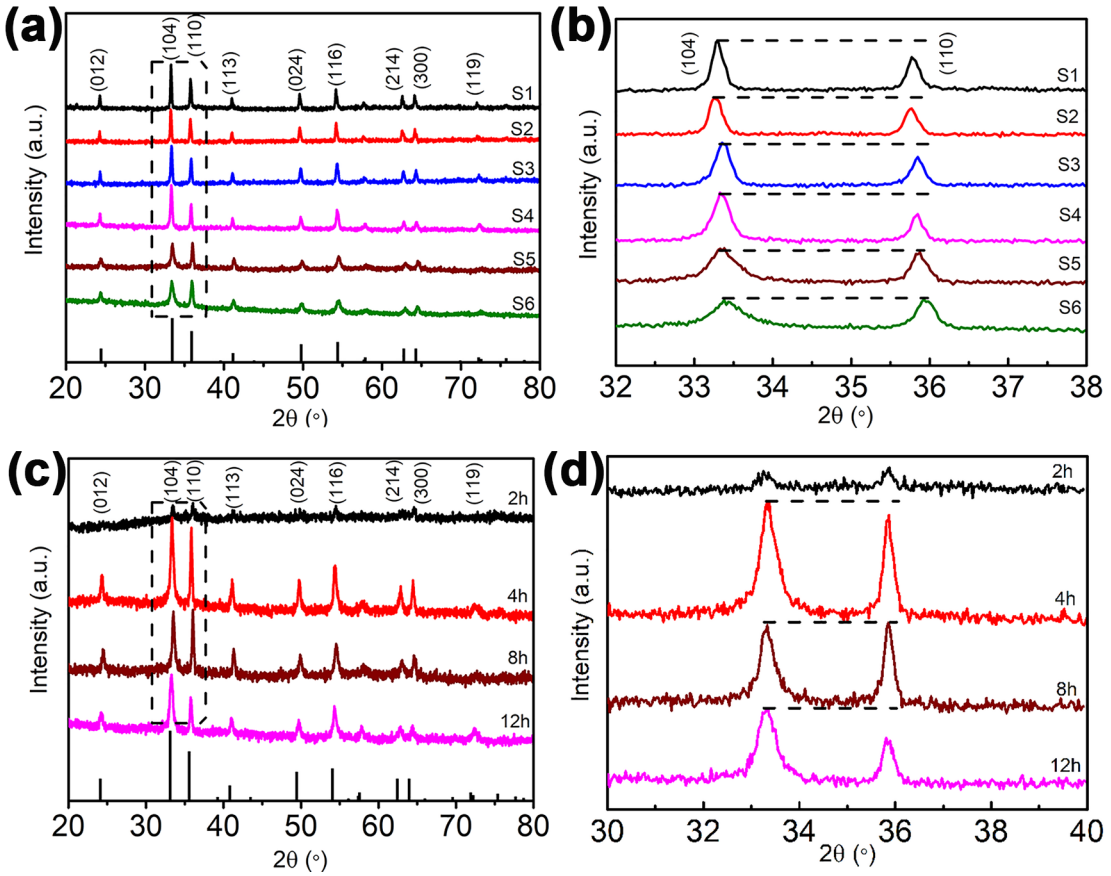

Figure 2. (a) XRD patterns of samples prepared under different Al^{3+} concentrations; (b) enlarged image of dotted box in panel (a); (c) XRD patterns of samples prepared under different hydrothermal treatment times; (d) enlarged image of dotted box in panel (c).

EDS detector. N_2 adsorption/desorption measurements were carried out at 77 K by using a Quantachrome instrument (Quabrasorb SI-3MP, US).

2.4. Electrochemical Property Tests. The electrodes were prepared by mixing 80 wt % active material, 10 wt % super P, and 10 wt % polyvinylidenefluoride in *N*-methyl-2-pyrrolidone to form a slurry, which was subsequently cast on copper foils. The as-prepared electrodes were then dried at 120 °C in vacuum for 12 h. The cells were assembled in a glovebox, using Li foil as both counter and reference electrodes, Celgard-2400 as separator, and 1.0 M $LiPF_6$ in ethylene carbonate/diethyl carbonate (1:1 by volume) as the electrolyte. Galvanostatic charge and discharge measurements were conducted between 0.01 and 3 V vs Li/Li^+ by using a LAND 2001A battery tester. Cyclic voltammetry (CV) measurements were carried out on an electrochemical workstation (CHI660D) in the potential range between 0.01 and 3 V vs Li/Li^+. Electrochemical impedance spectroscopy (EIS) was carried out on an electrochemical workstation (CHI660D) by applying an ac amplitude of 0.5 mV in a frequency range between 100 kHz and 0.01 Hz.

2.5. Simulation Details. First-principles calculations based on density functional theory (DFT) were performed via the Vienna ab initio simulation package (VASP)[28] by adopting projector augmented wave (PAW)[29] method with the Perdew–Burke–Ernzehof (PBE)[30] functional. The energy cutoff was set to 500 eV. The (7 × 7 × 2), (8 × 8 × 1), and (6 × 5 × 1) *k*-point meshes were used for Fe_2O_3 bulk, (001) surface, and (110) surface, respectively. The convergence tolerance for the force and energy during the structure relaxation were set to 0.01 eV/Å and 10^{-5} eV, respectively. The surfaces were described by a slab model with thicknesses of 6.00 and 4.94 Å for the (001) and (110) surfaces, respectively. The migration paths and energy barriers of lithium (Li) on Fe_2O_3 surface were studied by climbing image-nudged elastic band (cNEB) method,[31] which could more accurately find out the saddle points with fewer images than the original one. The initial and final states are the most stable adsorption sites of Li^+ on Fe_2O_3 surface, and the migration process with 5 images was adopted.

The surface free energy (E_{surf}) was calculated by eq 1:

$$E_{surf} = \frac{E_{slab} - nE_{bulk}}{2S} \quad (1)$$

where E_{bulk} is the per formula unit energy of bulk Fe_2O_3, E_{slab} is the energy of surface, the surface is created according to the stoichiometric ratio, and S is the area of the surface. The thickness of surface model is continuously increased until the change of surface free energy is less than 1%.

3. RESULTS AND DISCUSSION

The formation process of α-Fe_2O_3 with different morphologies (exposed facets) is shown in Figure 1. Figure 1a schematically shows that the addition of Al^{3+} in the reaction system plays an important role in the formation of α-Fe_2O_3 with various morphologies (exposed facets). As demonstrated by previous research work,[26] due to the high alkalinity of the reaction system, Al^{3+} ions can be dissolved into the solution and would exert the role of structure and surface director of product. Under synthetic conditions with a high concentration of $NH_3 \cdot H_2O$, extra Al^{3+} ions would be adsorbed to the α-Fe_2O_3 (001) surface and induce α-Fe_2O_3 nanoparticles to grow into hexagonal nanoplates. The structure evolution of α-Fe_2O_3 product was systematically investigated through SEM and the results shown in Figure 1b–g reveals an Al^{3+}-concentration-dependent mechanism for α-Fe_2O_3 growth. Without adding

DOI: 10.1021/acs.inorgchem.9b01626
Inorg. Chem. XXXX, XXX, XXX–XXX

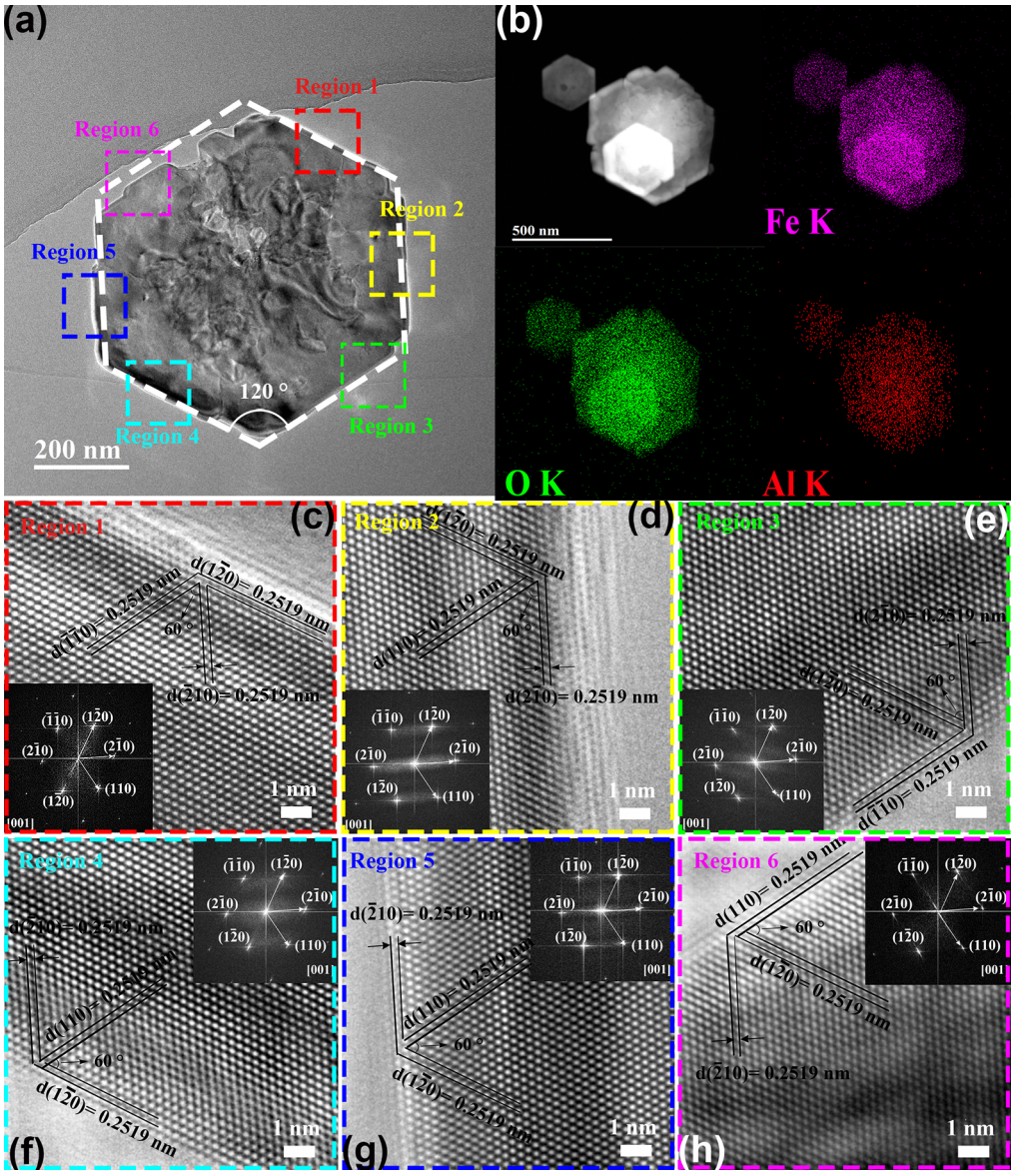

Figure 3. (a) TEM image of a single α-Fe_2O_3 (S5) hexagonal nanosheet. (b) EDX elemental mapping of α-Fe_2O_3 nanosheets; (c–h) HRTEM images of regions 1–6 of α-Fe_2O_3 nanosheet in panel (a), and the inset images show the corresponding SAED patterns.

any aluminum ions, uniform octahedral α-Fe_2O_3 products are obtained (see Figure 1b). The growth apex of octahedral α-Fe_2O_3 is limited when increasing the concentration of aluminum ions (S2 sample), resulting in irregular polygonal-like morphology (see Figure 1c). On further increasing the Al^{3+} concentration in the precursor solution, α-Fe_2O_3 becomes more regular and thinner (see Figure 1d,e). As for the S5 sample, α-Fe_2O_3 exhibits an ideal hexagonal-like nanosheet structure with a lateral size of approximately 400–600 nm (see Figure 1f). However, with continually increasing Al^{3+} concentration in the precursor solution, numerous nanoparticles emerge on the surface of α-Fe_2O_3 (see Figure 1g), and such nanoparticles could be impurities generated during the hydrothermal process. Moreover, the SEM images of α-Fe_2O_3 products (S5) synthesized under different hydrothermal durations have been provided in Figure S1, which indicate that the hydrothermal time significantly influences the purity and structural regularity of α-Fe_2O_3 hexagonal nanosheets.

A comparison of the XRD patterns of Fe_2O_3 products prepared under different Al ion concentrations is shown in Figure 2a,b. From Figure 2a, all XRD patterns of Fe_2O_3 samples (S1–S6) show highly intensive diffraction peaks at 2θ of 12.1, 16.6, 17.8, 20.4, 24.7,27.1, 31.2, 32, and 36.1°, which are attributed to the (012), (104), (110), (113), (024), (116), (214), (300), and (119) plane diffractions of the rhombohedral phase of hematite (Powder Diffraction File no. 33–0664, Joint Committee on Powder Diffraction Standards, 2004 year), indicating the well crystal structure of α-Fe_2O_3 products. More importantly, the peak-intensity ratios of (110)/(104) vary with different Al^{3+} concentrations (see Figure 2b). Specifically, the peak-intensity ratios of (110)/(104) of samples S1–S6 are 0.66, 0.71, 0.68, 0.56, 1.02, and 0.99, respectively. The higher intensity ratio of (110)/(104) indicates that α-Fe_2O_3 prefers to grow along the *a*-direction rather than along the *c*-direction, leading to the formation of exposed facets along the *a*-direction.[32] Additionally, samples S1–S6 show peak shifts corresponding to the (110) and (104)

DOI: 10.1021/acs.inorgchem.9b01626
Inorg. Chem. XXXX, XXX, XXX–XXX

facets, which is related to the variation of *d*-spacing of (110) and (104) facets. The *d*-spacing difference could be attributed to the absorption of Al^{3+} ion in the Fe_2O_3 structure, and a detailed investigation will be conducted in a future work. Moreover, XRD patterns of Fe_2O_3 synthesized under various hydrothermal durations of 2, 4, 8, and 12 h have been provided in Figure 2c,d. From Figure 2c, weak diffraction peaks shown in the XRD pattern of Fe_2O_3 prepared under 2 h indicate low crystallinity of the product. After 4 h, crystal α-Fe_2O_3 formed since intensive diffraction peaks are observed in the XRD pattern (the peak intensity of products prepared under 8 and 12 h seems to be mild compared to that of products prepared under 4 h, which could be attributed to the impurities present in the products), which are indexed to diffraction peaks of the rhombohedral phase of hematite. On the basis of calculation, the peak-intensity ratios of (110)/(104) of Fe_2O_3 prepared under different hydrothermal times from 4 to 12 h are 0.88, 1.02, and 0.62, respectively. The XRD results reveal that α-Fe_2O_3 (S5) prepared under an aluminum acetate basic mass of 48 mg and a hydrothermal time of 8 h prefers to grow along the *a*-direction rather than along the *c*-direction, leading to the preferential growth of facets parallel to *a*-direction.[32]

The microstructure of α-Fe_2O_3 hexagonal nanosheet (S5) has been further investigated by TEM. As shown in Figure 3a, a α-Fe_2O_3 nanosheet possesses an ideal hexagonal-like morphology. Such α-Fe_2O_3 nanosheets show a lateral size of approximately 600 nm with a thickness of 50 nm (Figure S2a,b), which is consistent with the SEM images. The different contrasts in TEM images between the middle and edge regions reveal a rough surface of the α-Fe_2O_3 nanosheet, which could be related to the experimental parameters during the preparation process. Figure 3b contains energy-dispersive X-ray spectrometry (EDX) elemental mappings of α-Fe_2O_3 nanosheets, indicating that Fe, O, and Al elements are uniformly distributed in nanosheets, which has also been confirmed by the XPS results in Figure S3. Moreover, the EDX mapping result in Figure S4 indicates the presence of Al in the final α-Fe_2O_3 product. The ICP results in Table S1 reveal the different Al contents in α-Fe_2O_3 products prepared under different Al ion concentrations in the precursor solution. To investigate the exposed facet of the α-Fe_2O_3 nanosheet, high-resolution TEM images of different regions (six sides of the hexagon in Figure 3a) of the nanosheet are provided in Figure 3c–h. In all regions, three sets of lattices are observed, and the lattice fringes are approximately 0.2519 nm, corresponding to the $d_{(110)}$ spacing of α-Fe_2O_3. The selected regions 1–6 correspond to the $(1\bar{2}0)$, $(2\bar{1}0)$, (110), $(\bar{1}20)$, $(\bar{2}10)$, and $(\bar{1}\bar{1}0)$ facets of α-Fe_2O_3, respectively, implying the lateral facets of α-Fe_2O_3 nanosheets are enclosed by a {110} facet and that the predominant exposed facet is the (001) facet. The corresponding selected-area electron diffraction (SAED) patterns (see the insets of Figure 3c–h) clearly show one set of sharp diffraction spots, indicating the single-crystal character of α-Fe_2O_3, and all diffraction spots are indexed to [001] axis (labeled in the insets of Figure 3c–h). The TEM results suggest that the α-Fe_2O_3 hexagonal nanosheet mainly has the (001) facet exposed. Moreover, the BET results of α-Fe_2O_3 (S5) (see Figure S6) indicate the mesoporous nature of the α-Fe_2O_3 nanosheets.

According to the above discussions, the resulting well-defined α-Fe_2O_3 hexagonal nanosheets with a predominantly (001) exposed facet are established by adding the suitable concentration of aluminum ions in the precursor solution and using a certain reaction time, and Al exerts an essential role to determine the morphology and exposed facet of α-Fe_2O_3 products. The intrinsic mechanism of forming α-Fe_2O_3 hexagonal nanosheets with (001) facet exposed is presented on the basis of first-principle calculations. The surface energies of different facet are calculated as listed in Table 1. Obviously,

Table 1. Surface Free Energy (KJ m^{-2})

surface	(001)	(110)	$(2\bar{1}0)$	$(1\bar{2}0)$
E_{surf}	1225	2628	2628	2628

the surface energy of a top-enclosed (001) facet is much lower than those of lateral {110} facets, indicating the (001) facet is more stable than these lateral facets. Moreover, the surface energy values of other typical facets of (104), (116), and (214) are 1238, 1299, and 1668 KJ m^{-2}, respectively, which are higher than that of (001) facet, further demonstrating the high stability of the (001) facet. The DFT results are provided as a reference.

The electrochemical performance of α-Fe_2O_3 nanosheet (S5) as LIB anode is systematically investigated, and the related results are shown in Figures 4 and S7. Figure 4a shows the charge/discharge curves of the α-Fe_2O_3 electrode during the first three cycles. The electrode exhibits a high discharge capacity of 1587.2 mAh g^{-1} and particularly a high capacity retention of approximately 80% (1261.3 mAh g^{-1}) after the first charge/discharge cycle. The initial irreversible capacity loss is much smaller than those values reported for contemporary LIB anodes.[21,33,34] Moreover, the charge/discharge curves of α-Fe_2O_3 anodes prepared under different Al ion concentrations (S1, S3, and S6) during the first three cycles have been provided in Figure S7, demonstrating the effect of Al ion concentration on the discharge capacity of α-Fe_2O_3 anodes. In this work, α-Fe_2O_3 nanosheets (S5) with largely exposed (001) facets provide rapid channels for Li-ion transfer, leading to high reversible capacity and relatively low initial-capacity loss (details discussed in section 2.5). Meanwhile, the capacity of electrode after first discharge process stabilizes around 1200 mAh g^{-1}, which demonstrates the high reversibility of the reaction.

Figure 4b displays specific capacities of electrode at various current densities ranging from 0.2 to 10 C (1 C = 1000 mA g^{-1}) and then back to 0.2 C to evaluate the rate performance of α-Fe_2O_3 anode. The α-Fe_2O_3 anode exhibits a high rate capability with a capacity retention of 71.5% (857.7 mAh g^{-1}) at 5 C and even a high capacity retention of over 50% (605 mAh g^{-1}) at 10 C. These results are substantially better than the reported rate capabilities of the state-of-the-art Fe-based electrodes, which fall in a capacity-retention range of 30–39% at 10 C (see Table S2). Normally, rate capability refers to the ability of electrodes to retain capacity at high charge/discharge rates (high charge/discharge current densities), which is a critical parameter for batteries that may determine their applicability in practical applications.[35,36] The excellent rate performance of the α-Fe_2O_3 anode could originate from the improved Li-ion-transfer performance across the (001) facets, which will be discussed in section 2.5. The long-term stability of α-Fe_2O_3 nanosheet (S5) was measured at a current density of 2 A g^{-1} over 500 cycles (see Figure 4c). During the first 50 cycles, the electrode undergoes a slight capacity attenuation, while experiences a continuous increase of capacity and subsequently stabilizes with a capacity of over 900 mAh g^{-1} at

DOI: 10.1021/acs.inorgchem.9b01626
Inorg. Chem. XXXX, XXX, XXX–XXX

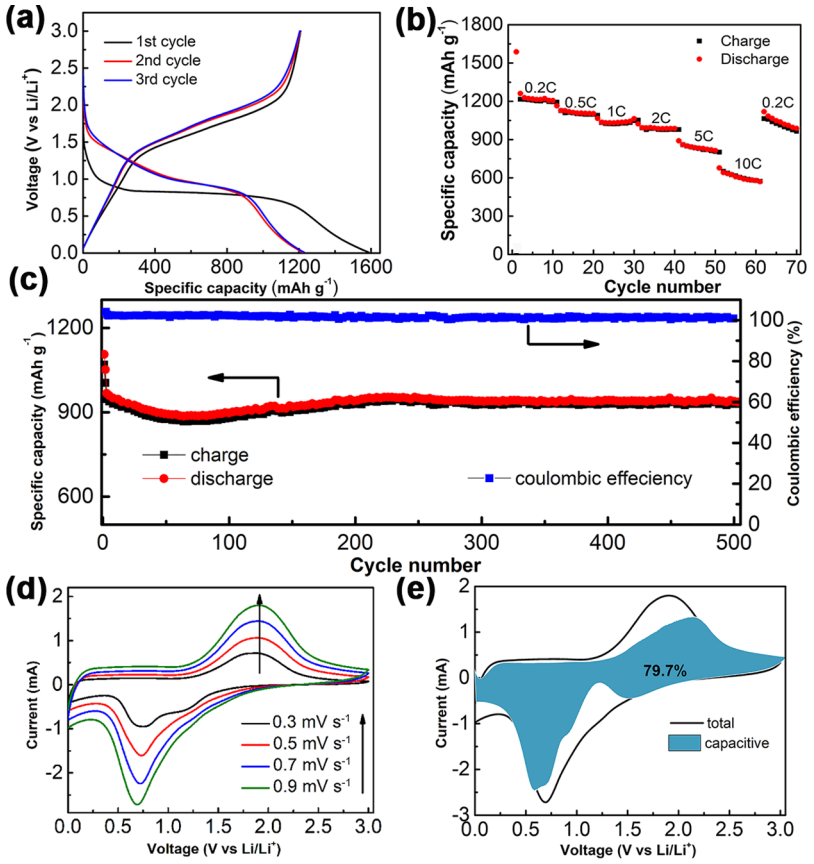

Figure 4. Electrochemical performance of α-Fe_2O_3 (S5 sample) as LIB anode: (a) Charge/discharge curves at a current density of 200 mA g^{-1} during first three cycles. (b) Rate performance at different current densities. (c) Long-term cyclability at a current density of 2 A g^{-1}. (d) CV curves at scan rates ranging from 0.3 to 0.9 mV s^{-1}. (f) Capacitive contribution at a scan rate of 0.9 mV s^{-1}.

500 cycles. Furthermore, cyclic stabilities of α-Fe_2O_3 anodes prepared under different Al ion concentrations (S1, S3, and S6) are evaluated under the same condition, and the results in Figure S7d indicates the superior cyclic stability of α-Fe_2O_3 nanosheet (S5) with large exposure of the (001) facet. The phenomenon of increased capacity has also been observed in many α-Fe_2O_3-based electrodes, which could be attributed to the activation process caused by electrolyte gradual wetting/soaking into electrode.[15,37] Moreover, the EIS result of the α-Fe_2O_3 nanosheet is provided in Figure S7b. The low charge-transfer resistance of the α-Fe_2O_3 nanosheets indicates small lithium ion migration resistance and the rapid migration of lithium ions.

To further understand the kinetics of the Li^+-transfer process, CV tests were conducted at different scan rates from 0.3 to 0.9 mV s^{-1}, and the results are shown in Figure 4d. The peak currents become higher with the increasing scan rate, and the peak voltages are almost independent of the scan rate, indicating the weak polarization effect of electrodes. The anodic and cathodic peak currents were fitted with the square root of the scan rate (see Figure S8), indicating the redox reaction is a diffusion-controlled process. The Li-ion diffusion coefficient could be calculated according to eq 2:[38,39]

$$I_p = 2.69 \times 10^5 n^{3/2} A (D_{Li})^{1/2} v^{1/2} C_0 \quad (2)$$

where I_p is the peak current, n is the electronic number participating in the reaction, A is the electrode area immersed in solution, D_{Li} is the Li-ion diffusion coefficient, v is scan speed, and C_0 is the bulk concentration of Li ion in electrode after the insertion reaction to evaluate diffusion coefficient. D_{Li} in α-Fe_2O_3 nanosheets (S5) is calculated to be 4.4×10^{-12} cm^2 s^{-1} (for calculation details, see Figure S8), which is in agreement with the values reported in previous research work.[40,41] Moreover, the relationship between scan rates and discharge peak currents of different samples (S1, S3, S5, and S6) is shown in Figure S9 and indicates the highest diffusion coefficient of α-Fe_2O_3 nanosheets (S5), further confirming the outstanding electrochemical performance of α-Fe_2O_3 nanosheets (S5).

Furthermore, the capacitive behavior of α-Fe_2O_3 which is related to its high rate capability and excellent cyclic stability[42,43] has been investigated in depth on the basis of CV curves at different scan rates. The total stored charge of the α-Fe_2O_3 anode is composed of three components: the faradaic contribution through Li^+ insertion, the faradaic contribution from charge transfer occurring within the surface (pseudocapacitance), and the double-layer capacitance. The capacitive contribution (both pseudocapacitance and double-layer capacitance) can be quantitatively measured through the CV curves under different scan rates. The current at a fixed potential can be expressed as the combination of two separate parts, surface capacitive behavior and diffusion-controlled insertion process, which follows the equation:[44]

$$I(V) = k_1 v + k_2 v^{1/2} \quad (3)$$

where v is the sweep rate and $k_1 v$ and $k_2 v^{1/2}$ correspond to the capacitive contribution and the Li^+ insertion contribution, respectively. Thus, by determining both k_1 and k_2, it is possible

DOI: 10.1021/acs.inorgchem.9b01626
Inorg. Chem. XXXX, XXX, XXX−XXX

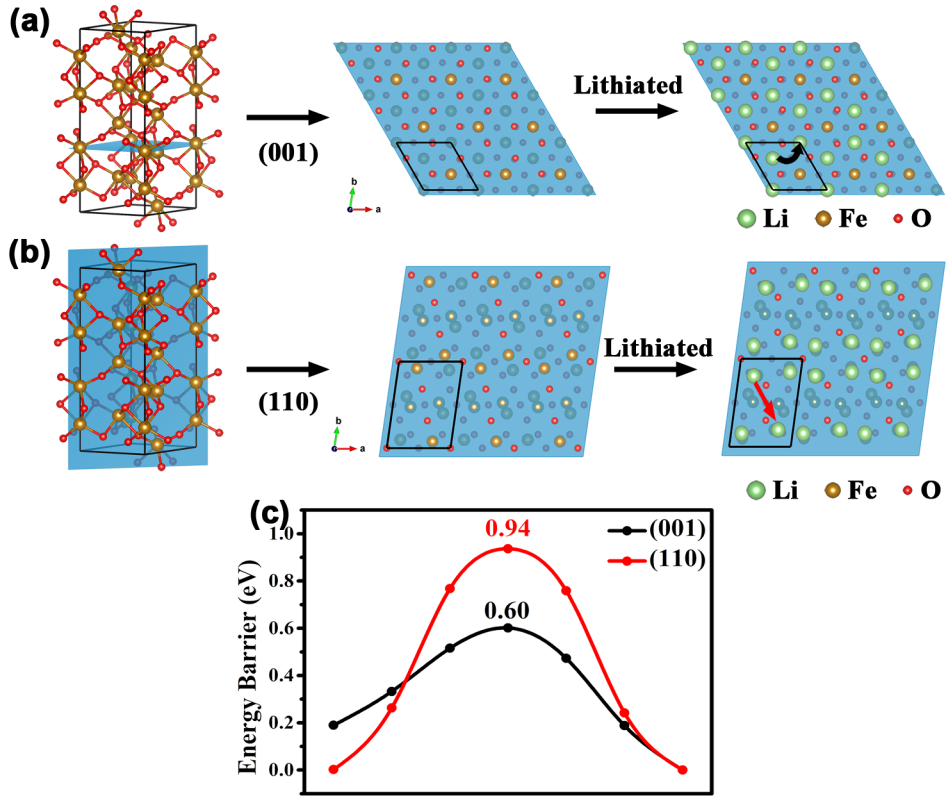

Figure 5. (a) Surface atomic configurations in the (001) plane and the corresponding lithium ion transfer path. (b) Surface atomic configurations in the (110) plane and the corresponding lithium ion transfer path. (c) Energy barriers of lithium ion transfer across the (001) and (110) facets.

to distinguish the fraction of the current originated from Li^+ insertion and that from capacitive processes at specific potentials.

As shown in Figure 4e, at a scan rate of 0.9 mV s^{-1}, the capacitive process contributes approximately 80% of the whole stored charge. Even at a low scan rate of 0.3 mV s^{-1}, 74% of the stored charge comes from the capacitive process (see Figure S10), which demonstrates the high capacitive contribution of the α-Fe_2O_3 anode during the energy-storage process. The high capacitive behavior of α-Fe_2O_3 anode has revealed that energy storage is mainly a surface-controlled process without limitations from solid-state diffusion, which is beneficial for the fast transfer of Li^+ across the engineered exposed facet, consequently leading to the high rate capability and outstanding cyclic stability of α-Fe_2O_3 anode.

To investigate in depth the mechanism of the facet-dependent-electrochemical performance of α-Fe_2O_3 anode, crystal models were set up, and energy barriers of Li^+ transfer across different facets are quantitatively measured (for simulation details, see the Experimental Section). Notably, the model is set up based on the microstructure of materials (e.g., atom occupation, crystal structure, etc.), and the effects of the macrostructure (e.g., morphology, doping, etc.) would not be taken into consideration. In this work, experiments combined with DFT simulation are employed to reveal the formation mechanism of the (001) facet and the mechanism of lithium ion transfer, and DFT results could provide an auxiliary method to explain the experimental phenomenon. As for (001) facet (shown in Figure 5a), due to the structural symmetry, a crystal unit containing one Fe atom and four O atoms (labeled as a black parallelogram in Figure 5a) was selected for detailed calculation and analysis. During the lithiation process, Li ion occupies the vacancy between three O atoms; meanwhile, the Fe and O atoms retain their own occupations, which keeps the structure stable during the Li-ion transfer process. The side-view image provided in Figure S11a confirms the stable structure during the lithiation process. The path for Li ions across the (001) facet (labeled as a black arrow in Figure 5a) indicates Li-ions transfer along three oxygen vacancies with a short path. For the (110) facet, a crystal unit containing two Fe atoms and six O atoms (labeled as a black parallelogram in Figure 5b) has also been chosen for analysis. During the lithiation process, the Li ion occupies the position of Fe, which leads to structural distortion and instability (see Figure S11b). The path for Li ions across the (110) facet (labeled as a red arrow in Figure 5b) suggests a relatively long pathway for Li-ion transfer compared to that for (001) facet. Moreover, the energy barriers for Li-ion transfer across the (001) and (110) facets are calculated (seven points were chosen for calculation), and plots of the energy barriers along typical paths have been provided in Figure 5c. The energy barrier for Li-ion transfer across the (001) facet is much lower than that across the (110) facet, indicating the (001) facet provides rapid channels for Li-ion transfer.

4. CONCLUSIONS

In summary, α-Fe_2O_3 hexagonal-like nanosheets with an engineered exposed (001) facet have been designed and fabricated through a facile hydrothermal process. The addition of Al^{3+} in the reaction system plays an important role in the formation of α-Fe_2O_3 with various morphologies and exposed facets, and α-Fe_2O_3 hexagonal-like nanosheets present a large exposure of (001) facets. For LIB application, such α-Fe_2O_3 nanosheets exhibit high reversible discharge capacity, high rate

DOI: 10.1021/acs.inorgchem.9b01626
Inorg. Chem. XXXX, XXX, XXX−XXX

capability, and excellent cyclic stability. The kinetics of the Li^+-transfer process was investigated to reveal a capacitor-like behavior of the α-Fe_2O_3 anode with almost 80% of the stored energy originating from the capacitive contribution (at a scan rate of 0.9 mV s^{-1}). Moreover, DFT simulations combined with the crystal model demonstrate the improved Li^+-transfer performance across the (001) facet with a low energy transfer barrier of 0.64 eV and short transfer paths. The present work opens a new way to design high-performance electrodes with controllable exposed facets for an energy-storage system and provides a deep understanding of the underlying mechanism of Li^+-transfer behavior across engineered exposed facets, which could be particularly well-suited for practical implementation such as electrochemical energy storage systems, catalysis, and chemical sensors.

■ ASSOCIATED CONTENT

Supporting Information

The Supporting Information is available free of charge on the ACS Publications website at DOI: 10.1021/acs.inorgchem.9b01626.

Detailed SEM, TEM, XPS, BET, electrochemical performances, and simulation results (PDF)

■ AUTHOR INFORMATION

Corresponding Authors

*E-mail: s.yang@qdu.edu.cn (S.Y.).
*E-mail: fanlizhen@ustb.edu.cn (L.Z.F.).

ORCID

Pingge He: 0000-0002-6369-253X
Zhengping Ding: 0000-0001-5275-5905
Peng Gao: 0000-0003-0860-5525
Li-Zhen Fan: 0000-0003-2270-4458

Notes

The authors declare no competing financial interest.

■ ACKNOWLEDGMENTS

We gratefully acknowledge the financial support received from the following sources: University Basic Research Fund of China (06500105), Postdoctoral Science Fund of China (11175360), National Natural Science Foundation of China (51532002, 51872027 and 51802297), Beijing Natural Science Foundation (L172023), and National Basic Research Program of China (2017YFE0113500).

■ REFERENCES

(1) Sun, H.; Ang, H. M.; Tadé, M. O.; Wang, S. Co_3O_4 nanocrystals with predominantly exposed facets: synthesis, environmental and energy applications. *J. Mater. Chem. A* **2013**, *1* (46), 14427−14442.

(2) Sajan, C. P.; Wageh, S.; Al-Ghamdi, A. A.; Yu, J.; Cao, S. TiO_2 nanosheets with exposed {001} facets for photocatalytic applications. *Nano Res.* **2016**, *9* (1), 3−27.

(3) He, P.; Huang, B.; Huang, Q.; Chen, T.; Zhang, Q. Structural evolution of vertically oriented graphene nanosheet templating Ni−Co hydroxide as pseudocapacitive electrode. *J. Mater. Sci.* **2018**, *53* (17), 12352−12364.

(4) Liu, Y.; Chen, W.; Yang, C.; Wei, Q.; Wei, M. Hierarchical TiO_2-B composed of nanosheets with exposed {010} facets as a high-performance anode for lithium ion batteries. *J. Power Sources* **2018**, *392*, 226−231.

(5) Chen, J. S.; Tan, Y. L.; Li, C. M.; Cheah, Y. L.; Luan, D.; Madhavi, S.; Boey, F. Y. C.; Archer, L. A.; Lou, X. W. Constructing hierarchical spheres from large ultrathin anatase TiO_2 nanosheets with nearly 100% exposed (001) facets for fast reversible lithium storage. *J. Am. Chem. Soc.* **2010**, *132* (17), 6124−6130.

(6) He, P.; Huang, Q.; Huang, B.; Chen, T. Controllable synthesis of Ni−Co−Mn multi-component metal oxides with various morphologies for high-performance flexible supercapacitors. *RSC Adv.* **2017**, *7* (39), 24353−24358.

(7) Xu, G.-L.; Li, J.-T.; Huang, L.; Lin, W.; Sun, S.-G. Synthesis of Co_3O_4 nano-octahedra enclosed by {111} facets and their excellent lithium storage properties as anode material of lithium ion batteries. *Nano Energy* **2013**, *2* (3), 394−402.

(8) Chen, J. S.; Lou, X. W. SnO2-based nanomaterials: synthesis and application in lithium-ion batteries. *Small* **2013**, *9* (11), 1877−1893.

(9) Wang, X.; Cao, X.; Bourgeois, L.; Guan, H.; Chen, S.; Zhong, Y.; Tang, D. M.; Li, H.; Zhai, T.; Li, L.; et al. N-doped graphene-SnO_2 sandwich paper for high-performance lithium-ion batteries. *Adv. Funct. Mater.* **2012**, *22* (13), 2682−2690.

(10) Liu, X.; Liu, G.; Wang, L.; Li, Y.; Ma, Y.; Ma, J. Morphology- and facet-controlled synthesis of CuO micro/nanomaterials and analysis of their lithium ion storage properties. *J. Power Sources* **2016**, *312*, 199−206.

(11) He, P.; Zhao, K.; Huang, B.; Zhang, B.; Huang, Q.; Chen, T.; Zhang, Q. Mechanically robust and size-controlled MoS_2/graphene hybrid aerogels as high-performance anodes for lithium-ion batteries. *J. Mater. Sci.* **2018**, *53* (6), 4482−4493.

(12) Wang, L.; Nie, Z.; Cao, C.; Khalid, S.; Wu, Y.; Xu, X. Carbon-wrapped TiO_2 nanocubes exposed with (001) active facets for high-rate and long-life lithium-ion batteries. *J. Power Sources* **2016**, *302*, 259−265.

(13) Wu, Y.; Cao, C.; Zhang, J.; Wang, L.; Ma, X.; Xu, X. Hierarchical $LiMn_2O4$ hollow cubes with exposed {111} planes as high-power cathodes for lithium-ion batteries. *ACS Appl. Mater. Interfaces* **2016**, *8* (30), 19567−19572.

(14) Reddy, M.; Yu, T.; Sow, C.-H.; Shen, Z. X.; Lim, C. T.; Subba Rao, G.; Chowdari, B. α-Fe2O3 nanoflakes as an anode material for Li-ion batteries. *Adv. Funct. Mater.* **2007**, *17* (15), 2792−2799.

(15) Cao, K.; Jiao, L.; Liu, H.; Liu, Y.; Wang, Y.; Guo, Z.; Yuan, H. 3D hierarchical porous α-Fe_2O_3 nanosheets for high-performance lithium-ion batteries. *Adv. Energy Mater.* **2015**, *5* (4), 1401421.

(16) Cho, J. S.; Hong, Y. J.; Kang, Y. C. Design and synthesis of bubble-nanorod-structured Fe_2O_3−carbon nanofibers as advanced anode material for Li-ion batteries. *ACS Nano* **2015**, *9* (4), 4026−4035.

(17) Wang, L.; Lou, Z.; Deng, J.; Zhang, R.; Zhang, T. Ethanol gas detection using a yolk-shell (core-shell) α-Fe_2O_3 nanospheres as sensing material. *ACS Appl. Mater. Interfaces* **2015**, *7* (23), 13098−13104.

(18) Lupan, O.; Postica, V.; Wolff, N.; Polonskyi, O.; Duppel, V.; Kaidas, V.; Lazari, E.; Ababii, N.; Faupel, F.; Kienle, L.; Adelung, R. Localized synthesis of iron oxide nanowires and fabrication of high performance nanosensors based on a single Fe_2O_3 nanowire. *Small* **2017**, *13* (16), 1602868.

(19) Balogun, M.-S.; Wu, Z.; Luo, Y.; Qiu, W.; Fan, X.; Long, B.; Huang, M.; Liu, P.; Tong, Y. High power density nitridated hematite (α-Fe_2O_3) nanorods as anode for high-performance flexible lithium ion batteries. *J. Power Sources* **2016**, *308*, 7−17.

(20) Chen, M.; Liu, J.; Chao, D.; Wang, J.; Yin, J.; Lin, J.; Jin Fan, H.; Xiang Shen, Z. Porous α-Fe_2O_3 nanorods supported on carbon nanotubes-graphene foam as superior anode for lithium ion batteries. *Nano Energy* **2014**, *9*, 364−372.

(21) Zhang, G.; Shi, Y.; Wang, H.; Jiang, L.; Yu, X.; Jing, S.; Xing, S.; Tsiakaras, P. A facile route to achieve ultrafine Fe_2O_3 nanorods anchored on graphene oxide for application in lithium-ion battery. *J. Power Sources* **2019**, *416*, 118−124.

(22) Gao, G.; Zhang, Q.; Cheng, X.-B.; Qiu, P.; Sun, R.; Yin, T.; Cui, D. CNTs in situ attached to α-Fe_2O_3 submicron spheres for enhancing lithium storage capacity. *ACS Appl. Mater. Interfaces* **2015**, *7* (1), 340−350.

(23) Huang, P.; Tao, W.; Wu, H.; Li, X.; Yin, T.; Zhang, Q.; Qi, W.; Gao, G.; Cui, D. N-doped coaxial CNTs@ α-Fe_2O_3@ C nanofibers as

DOI: 10.1021/acs.inorgchem.9b01626
Inorg. Chem. XXXX, XXX, XXX−XXX

anode material for high performance lithium ion battery. *J. Energy Chem.* **2018**, *27* (5), 1453−1460.
(24) Kong, H.; Lv, C.; Yan, C.; Chen, G. Engineering mesoporous single crystals Co-doped Fe_2O_3 for high-performance lithium ion batteries. *Inorg. Chem.* **2017**, *56* (14), 7642−7649.
(25) Zhao, Y.; Yan, D.; Ding, C.; Su, D.; Ge, Y.; Zhao, Y.; Zhou, H.; Li, J.; Jin, H. Fe_2O_3 nanocubes exposed (012) active facets combination with graphene rendering enhanced lithium storage capability. *J. Power Sources* **2016**, *327*, 658−665.
(26) Liu, R.; Jiang, Y.; Lu, Q.; Du, W.; Gao, F. Al 3+ -controlled synthesis and magnetic property of α-Fe 2 O 3 nanoplates. *CrystEngComm* **2013**, *15* (3), 443−446.
(27) Wu, W.; Yang, S.; Pan, J.; Sun, L.; Zhou, J.; Dai, Z.; Xiao, X.; Zhang, H.; Jiang, C. Metal ion-mediated synthesis and shape-dependent magnetic properties of single-crystalline α-Fe $_2$ O $_3$ nanoparticles. *CrystEngComm* **2014**, *16* (25), 5566−5572.
(28) Kresse, G.; Furthmüller, J. Efficiency of ab-initio total energy calculations for metals and semiconductors using a plane-wave basis set. *Comput. Mater. Sci.* **1996**, *6* (1), 15−50.
(29) Kresse, G.; Joubert, D. From ultrasoft pseudopotentials to the projector augmented-wave method. *Phys. Rev. B: Condens. Matter Mater. Phys.* **1999**, *59* (3), 1758.
(30) Perdew, J. P.; Burke, K.; Ernzerhof, M. Generalized gradient approximation made simple. *Phys. Rev. Lett.* **1996**, *77* (18), 3865.
(31) Henkelman, G.; Uberuaga, B. P.; Jónsson, H. A climbing image nudged elastic band method for finding saddle points and minimum energy paths. *J. Chem. Phys.* **2000**, *113* (22), 9901−9904.
(32) Ouyang, J.; Pei, J.; Kuang, Q.; Xie, Z.; Zheng, L. Supersaturation-controlled shape evolution of α-Fe_2O_3 nanocrystals and their facet-dependent catalytic and sensing properties. *ACS Appl. Mater. Interfaces* **2014**, *6* (15), 12505−12514.
(33) Li, Y.; Huang, Y.; Zheng, Y.; Huang, R.; Yao, J. Facile and efficient synthesis of α-Fe_2O_3 nanocrystals by glucose-assisted thermal decomposition method and its application in lithium ion batteries. *J. Power Sources* **2019**, *416*, 62−71.
(34) Zhang, J.; Sun, Y.; Yao, Y.; Huang, T.; Yu, A. Lysine-assisted hydrothermal synthesis of hierarchically porous Fe_2O_3 microspheres as anode materials for lithium-ion batteries. *J. Power Sources* **2013**, *222*, 59−65.
(35) Zhao, K.; Zhang, L.; Xia, R.; Dong, Y.; Xu, W.; Niu, C.; He, L.; Yan, M.; Qu, L.; Mai, L. SnO_2 Quantum dots@ graphene oxide as a high-rate and long-life anode material for lithium-ion batteries. *Small* **2016**, *12* (5), 588−594.
(36) Zhang, Y.; Rui, X.; Tang, Y.; Liu, Y.; Wei, J.; Chen, S.; Leow, W. R.; Li, W.; Liu, Y.; Deng, J.; et al. Wet-Chemical Processing of Phosphorus Composite Nanosheets for High-Rate and High-Capacity Lithium-Ion Batteries. *Adv. Energy Mater.* **2016**, *6* (10), 1502409.
(37) Lee, S. H.; Yu, S.-H.; Lee, J. E.; Jin, A.; Lee, D. J.; Lee, N.; Jo, H.; Shin, K.; Ahn, T.-Y.; Kim, Y.-W.; et al. Self-assembled Fe3O4 nanoparticle clusters as high-performance anodes for lithium ion batteries via geometric confinement. *Nano Lett.* **2013**, *13* (9), 4249−4256.
(38) Ding, N.; Xu, J.; Yao, Y.; Wegner, G.; Fang, X.; Chen, C.; Lieberwirth, I. Determination of the diffusion coefficient of lithium ions in nano-Si. *Solid State Ionics* **2009**, *180* (2−3), 222−225.
(39) Tang, S.; Lai, M.; Lu, L. Study on Li+-ion diffusion in nano-crystalline $LiMn_2O_4$ thin film cathode grown by pulsed laser deposition using CV, EIS and PITT techniques. *Mater. Chem. Phys.* **2008**, *111* (1), 149−153.
(40) Penki, T. R.; Shivakumara, S.; Minakshi, M.; Munichandraiah, N. Porous Flower-like α-Fe_2O_3 Nanostructure: A High Performance Anode Material for Lithium-ion Batteries. *Electrochim. Acta* **2015**, *167*, 330−339.
(41) Cao, Z.; Wei, B. α-Fe2O3/single-walled carbon nanotube hybrid films as high-performance anodes for rechargeable lithium-ion batteries. *J. Power Sources* **2013**, *241*, 330−340.
(42) Augustyn, V.; Come, J.; Lowe, M. A.; Kim, J. W.; Taberna, P.-L.; Tolbert, S. H.; Abruña, H. D.; Simon, P.; Dunn, B. High-rate electrochemical energy storage through Li+ intercalation pseudocapacitance. *Nat. Mater.* **2013**, *12* (6), 518.
(43) Augustyn, V.; Simon, P.; Dunn, B. Pseudocapacitive oxide materials for high-rate electrochemical energy storage. *Energy Environ. Sci.* **2014**, *7* (5), 1597−1614.
(44) Liu, T. C.; Pell, W.; Conway, B.; Roberson, S. Behavior of molybdenum nitrides as materials for electrochemical capacitors comparison with ruthenium oxide. *J. Electrochem. Soc.* **1998**, *145* (6), 1882−1888.

DOI: 10.1021/acs.inorgchem.9b01626
Inorg. Chem. XXXX, XXX, XXX−XXX